Design of a high fidelity Fluid-Structure Interaction solver using LES on unstructured grid

T. Fabbri, G. Balarac, V. Moureau, P. Benard

Design of a high fidelity Fluid-Structure Interaction solver using LES on unstructured grid

T. Fabbri[a], G. Balarac[a,b], V. Moureau[c], P. Benard[c]

[a] *Université Grenoble-Alpes, Grenoble-INP, CNRS, LEGI, 38000 Grenoble, France*
[b] *Institut Universitaire de France (IUF), Paris, France*
[c] *Normandie Univ, INSA Rouen, UNIROUEN, CNRS, CORIA, 76000 Rouen, France*

Abstract

Despite promising experimental works, high fidelity numerical simulations of chordwise flexible blade are useful to better understanding. However, such simulation remains a challenging problem as it requires a Fluid-Structure Interaction (FSI) solver capable of accurately predicting the stall dynamics, while computing the deformation of a solid with complex geometry. In this paper, the authors propose a LES-based FSI solver using 3D solid elements for the solid and unstructured grid for fluid and solid solvers. This approach aims at being universal and is based on a partitioned coupling scheme, allowing low density ratios of the structure to the fluid. It uses an original pseudo-solid method for the mesh movement solving, specifically developed for this work. Besides, this solver is suited for massively parallel computing and can perform Dynamic Mesh Adaptation to be able to take into account any solid movement. Both fluid and solid solvers are validated independently before validation of the FSI solver against a 2D laminar benchmark, including mesh convergence study. The entire methodology is then successfully applied to experimental 3D complex case with high Reynolds number, confirming the potential of the FSI solver for its intended use, without geometry restriction. This is finally illustrated with a simulation of an experiment involving a chordwise flexible blade with large deformation, which has never been reproduced with a 3D LES approach in litterature so far.

Keywords: Fluid-Structure Interaction, Large-Eddy Simulation, Finite Element Method, Unstructured grid, Dynamic Mesh Adaptation, Mesh movement, Pseudo-solid, Partitioned scheme, Chordwise flexible foil

1. Introduction

Fluid-Structure Interaction (FSI) phenomena are very common in nature and human activities. It happens as soon as a fluid and a solid are in contact and that the solid is deformed significantly under the effect of the forces applied by the fluid. The structure displacement influences also the flow, resulting in a complex coupling process [1]. Examples in nature include wings of birds and insects interacting with surrounding air, or fish swimming [2]. In order to get a better understanding of these problems, numerical simulations of FSI cases have been developed substantially in the last decade. This has been made possible by recent increases in the available computational resources, but it is still very challenging because it requires specific solvers in different physics fields. Thus, FSI simulations use has spread to bio-medicine and even civil engineering [3]. FSI simulations can also be useful to design efficiently aircraft wings, drone wings or turbine blades.

A recent review of fluid dynamics of flapping and pitching foils [4] shows that even if the interest in the subject is growing since the last fifteen years, most of the studies focused on rigid foil. Only a few involved flexible foil, and they mainly concerned experimental works, showing that it is still very difficult to numerically reproduce the FSI case of a chordwise flexible foil with high fidelity. However, Hoerner et al. [5, 6] showed in recent experimental studies that in the operational characteristics of a Vertical Axis Turbine (VAT), blades with high flexibility deliver significantly higher torque and can reduce structural loads, extending turbine lifetime. These potential improvements of turbine efficiency seem to be explained by the influence of the chordwise flexibility on dynamic stall which implies a drag reduction.

To simulate cases of that kind, a high fidelity FSI solver is required. Such tool must be able to handle cases with turbulence and complex geometries, for the fluid as well as for the solid. This involves a FSI solver with different characteristics:

- For the flow solving, it is essential to correctly capture the velocity gradients close to the blade, which can be difficult with techniques based on immersed boundaries [7], given that the interpolations near the interface can be a source of error [8]. Besides, as a fine description of boundary layer at high Reynolds number requires small cell sizes, ensure the com-

putation accuracy in cases with large structure displacements involves a fine grid resolution in an extended region. The necessary large amount of cells would induce prohibitively high computational cost. On the contrary, body fitted techniques do not suffer from these deficiencies, but require a mesh movement computation.

- In regard to the computation of the structure deformation, several methods exist, generally based on different types of finite element. Nonetheless, accurately describe the foil geometry and internal stress, especially in cases of chordwise flexibility, implies a solid solver that can use 3D solid elements, where FSI solvers sometimes prefer to use membrane or shell elements [9, 10]. These elements are highly adapted to reproduce the structure behaviour with the corresponding geometry, but do not allow to reproduce structures with more complex geometry, such as a foil.

- Furthermore, flexible blades are composed by material with density comparable with the water density, implying that the FSI coupling can be very unstable and requires a strong coupling [11]. A monolithic approach can overcome this issue [12], but this solution lacks adaptability, so that a partitioned scheme is favored in most of recent studies [13]. This method allows to fully benefit of highly advanced solvers for both fields of application [8].

These requirements explain the limited number of numerical studies concerning flexible foil. However, some FSI solvers have been developed to face this challenge. For instance, MacPhee et al. [14] managed to simulate a three flexible blades turbine using the Unsteady Reynolds-Averaged Navier-Stokes (URANS) approach with the k-ω-SST model for turbulence. They found an increase of power coefficients around 9.6% in comparison to the same turbine with rigid blade. Similar method has been used by Marinić-Kragić et al. [15] to reproduce a Savonius-type wind turbine and they also found an additional 8% increase in the power coefficient. Nevertheless, Reynolds-Averaged Navier-Stokes (RANS) based FSI solvers do not always provide reliable results, because the pressure distribution is not accurate enough to conveniently determine dynamic stall separation point position. This is why Hoerner et al. [5] suggest that three-dimensional Large-Eddy Simulations (LES) approach is required to reproduce with high fidelity a high Reynolds number case involving a chordwise flexible

blade.

As detailed in [16], LES-based FSI solvers face different issues, because they demand higher grid quality than RANS approach and impose a fine time and space resolution. When this mesh resolution changes over time because of the deformations of the fluid domain, additional errors arise due to the lack of commutation between the time and space partial derivatives, and the filtering. These time and space commutation errors have been largely studied [17, 18] and they impose to have smooth variations of the filter width in both space and time. Also, the moving grid quality can be difficult to maintain, as it requires robust and efficient mesh movement method, especially for unstructured grids. Very few LES-based FSI solvers have been developed [16, 19, 20, 21], but they never use 3D solid elements, making a chordwise flexible foil simulation impossible.

To the best of authors' knowledge, LES-based FSI solvers meeting all the previous requirements do not exist in the literature so far. That is why the motivation of this study is to present the design of a high fidelity FSI solver, able to reproduce a wide variety of FSI configurations. It uses a LES solver based on Finite Volume Method (FVM) for the flow and Finite Element Method (FEM) for the structure displacement prediction, with unstructured grids for both domains. This approach allows the numerical simulation of 3D turbulent FSI cases, without geometry restriction, even implying large deformations. For that, an original mesh movement method based on pseudo-solid approach coupled with Dynamic Mesh Adaptation (DMA) has been developed. Besides, it is based on a partitioned coupling scheme, allowing low density ratios of the structure to the fluid. This paper is organized as follows. After a brief presentation of the numerical methodology used for both fluid and solid fields in section 2, a focus is performed in section 3 on the original method developed for the unstructured fluid mesh movement. In section 4, the FSI coupling scheme is explained in details. The present FSI solver is then validated on a 2D laminar (section 5) and a 3D turbulent benchmarks (section 6). Finally, an experiment involving a chordwise flexible blade is simulated in section 7.

2. Numerical methodology

All the present work has been performed based on the YALES2 library [22]. It can handle structured or unstructured meshes with a high number of elements thanks to a double domain decomposition. At first, the mesh is partitioned into

sub-parts which are affected to each computational core. Then, the sub-parts are split again into cell group of prescribed size. This technique allows for easily optimizing the use of processor memory with cache-aware algorithms and may also be exploited by deflation algorithms [23], in order to fully benefit from high-performance computing on massively parallel machines.

2.1. Computational Fluid Dynamics (CFD) solver

The equations describing the flow dynamics are the Navier-Stokes equations. To take into account moving bodies, the Arbitrary-Lagrangian-Eulerian (ALE) approach is used. With the latter, which consists in integrating the governing equations on deformable control volumes, nodes of the computational mesh are moved as Lagrangian points. In order to express the modified Navier-Stokes equation in the ALE framework, the material time derivative has to be defined. If nodes are moved at a velocity $\dot{\mathbf{x}}$, then the material time derivative can be written as

$$\frac{\mathrm{d}\mathbf{u}}{\mathrm{d}t} = \frac{\partial \mathbf{u}}{\partial t} + \mathbf{c} \cdot \nabla \mathbf{u}\,, \tag{1}$$

where $\mathbf{c} = \mathbf{u} - \dot{\mathbf{x}}$ is the relative velocity between material and mesh points. Thus, the governing equations can be rewritten as follow

$$\frac{\partial \mathbf{u}}{\partial t} + (\mathbf{c} \cdot \nabla)\mathbf{u} = -\frac{\nabla P}{\rho_f} + \nu \Delta \mathbf{u} + \nabla \cdot \boldsymbol{\tau}^{\mathbf{SGS}} + \mathbf{g}\,, \tag{2}$$

$$\nabla \cdot \mathbf{u} = 0\,, \tag{3}$$

where $\mathbf{u}$ is the vector field of material velocity, P the pressure, ρ_f the fluid density, ν the kinematic viscosity, $\boldsymbol{\tau}^{SGS}$ the sub-grid scale (SGS) stress tensor in LES approach and $\mathbf{g}$ the gravitational acceleration. Additional details for the ALE technique can be found in [24] and its implementation in the YALES2 framework in [25]. In the ALE solver, a FVM with a central 4th-order numerical scheme is used for spatial discretization. For the sake of clarity, next equations in this part are written without SGS stress tensor and without the gravitational acceleration.

Eq. (2) are solved by using a projection method for pressure-velocity coupling [26]. It consists in a "velocity prediction" step, which allows to compute an intermediate velocity $\mathbf{u}^*_{\mathrm{n}+1}$ from the given velocity $\mathbf{u}_{\mathrm{n}}$ by integration of the Navier-Stokes equations without the pressure term. In the ALE approach, and by using the first order explicit Euler time advancement scheme for simplicity,

this step reads,

$$\frac{\mathbf{u}^*_{\mathrm{n}+1} - \mathbf{u}_{\mathrm{n}}}{\Delta t} = -(\mathbf{c}_{\mathrm{n}} \cdot \nabla)\mathbf{u}_{\mathrm{n}} + \nu \nabla^2 \mathbf{u}_{\mathrm{n}} \,. \tag{4}$$

In YALES2, a 4th-order Runge–Kutta scheme is used for time advancement [27]. The velocity at the end of the time-step, $\mathbf{u}_{\mathrm{n}+1}$, is then related to the intermediate one, $\mathbf{u}^*_{\mathrm{n}+1}$, by

$$\frac{\mathbf{u}_{\mathrm{n}+1} - \mathbf{u}^*_{\mathrm{n}+1}}{\Delta t} = -\frac{\nabla P_{\mathrm{n}+\frac{1}{2}}}{\rho_f} \,. \tag{5}$$

Taking the divergence of Eq. (5) and considering that $\mathbf{u}_{\mathrm{n}+1}$ has to satisfy the divergence free condition, the Poisson equation is obtained

$$\Delta P_{\mathrm{n}+\frac{1}{2}} = \frac{\rho_f}{\Delta t} \nabla \cdot \mathbf{u}^*_{\mathrm{n}+1}. \tag{6}$$

This linear system is solved using a Deflated Preconditionned Conjugate Gradient (DPCG) solver [23]. Finally, the last step is the "velocity correction" step where the newly obtained pressure field $P_{n+\frac{1}{2}}$ is used to correct $\mathbf{u}^*_{\mathrm{n}+1}$ by solving Eq. (5).

It must also be noted that the integration volume Ω is chosen so that it verifies:

$$V_{\mathrm{n}+1} - V_{\mathrm{n}} = \Delta t \int_{\Omega} \nabla \cdot \dot{\mathbf{x}}_{\mathrm{n}+1} \, \mathrm{d}\Omega \,, \tag{7}$$

where V_{n} is the control volume at time t_{n}. This relation, known as the Discrete Geometric Conservation Law (DGCL) [28, 29], states that for each control volume, the volume change between t_{n} and $t_{\mathrm{n}+1}$ must be equal to the volume swept by the control volume faces during Δt.

2.2. Computational Structural Mechanics (CSM) solver

The equilibrium equation governing the solid dynamics can be written in a Lagrangian frame such as:

$$\rho_s \frac{\partial^2 \mathbf{d}}{\partial t^2} = \nabla \cdot \sigma + \mathbf{b} \,. \tag{8}$$

Here, ρ_s refers to the solid density, $\mathbf{d}$ the displacement, σ the Cauchy stress and $\mathbf{b}$ the body force applied on the solid. In the Structural Mechanics Solver (SMS), a classical finite element framework is used for spatial discretization, with second-order 2D or 3D solid elements like 9-nodes quadrilateral or 27-nodes hexahedron. This choice of element for FSI coupling framework, combined with unstructured grid solver for the fluid side, gives the possibility to consider a

broader range of FSI configurations.

With a finite element formulation, Eq. (8) becomes [30]:

$$\mathbf{M}\frac{\partial^2 \mathbf{d}}{\partial t^2} + \int_\Omega \hat{\mathbf{B}}^T \mathbf{S}\, \mathrm{d}\Omega = \mathbf{f} \tag{9}$$

where $\mathbf{M}$ is the mass matrix, $\hat{\mathbf{B}}$ the strain-displacement matrix, $\mathbf{S}$ the second Piola-Kirchhoff stress and Ω the domain in the reference configuration. Here, $\mathbf{d}$ and $\mathbf{f}$ are vectors that contain displacements and forces of each domain node, including the hydrodynamic forces at the solid boundaries in FSI cases. As Ω, $\hat{\mathbf{B}}$ and $\mathbf{S}$ depend on the deformation state, Eq. (9) can be noted

$$\mathbf{M}\ddot{\mathbf{d}}_{\mathrm{n}+1} + \mathbf{P}(\mathbf{d}_{\mathrm{n}+1}) = \mathbf{f}_{\mathrm{n}+1} \tag{10}$$

at each discrete time $t_{\mathrm{n}+1}$. To solve this non-linear equation, a Newton-Raphson method is applied here, so that the problem becomes the minimization of the function $\mathbf{\Psi}$ written

$$\mathbf{\Psi}(\mathbf{d}_{\mathrm{n}+1}) = \mathbf{f}_{\mathrm{n}+1} - \mathbf{M}\ddot{\mathbf{d}}_{\mathrm{n}+1} - \mathbf{P}(\mathbf{d}_{\mathrm{n}+1})\,. \tag{11}$$

To the first order, this equation can be approximated as

$$\mathbf{\Psi}(\mathbf{d}^{i+1}_{\mathrm{n}+1}) \approx \mathbf{\Psi}(\mathbf{d}^{i}_{\mathrm{n}+1}) + \left(\frac{\partial \mathbf{\Psi}}{\partial \mathbf{d}}\right)^{i}_{\mathrm{n}+1} d\mathbf{d}^{i}_{\mathrm{n}+1} = 0 \tag{12}$$

with i the Newton iteration counter. Thus, one Newton iteration consists in solving Eq. (12) and find the displacement increment $d\mathbf{d}$. To this purpose, the tangent stiffness matrix $\mathbf{K}_T$ has to be computed as

$$\begin{cases} \mathbf{K}_T = \dfrac{\partial \mathbf{P}}{\partial \mathbf{d}} & \text{(13a)} \\ \mathbf{K}^{ab}_T = \displaystyle\int_\Omega \hat{\mathbf{B}}^T_a \mathbf{D}_T \hat{\mathbf{B}}_b \mathrm{d}\Omega + \mathrm{G}_{ab}\mathbf{I} & \text{(13b)} \end{cases}$$

where $\mathbf{I}$ is the identity matrix and G_{ab}, the geometric stiffness term, can be written

$$\mathrm{G}_{ab} = \int_\Omega N_{a,I} S_{IJ} N_{b,J} \mathrm{d}\Omega\,. \tag{14}$$

In Eq. (13b), $\mathbf{D}_T$ is the matrix of tangent moduli, deduced from the constant elastic moduli $\mathbb{C}_{IJKL}$.

With the Saint-Venant-Kirchhoff model [30] used here, the stress-strain relation is

$$S_{IJ} = \mathbb{C}_{IJKL} E_{KL} \tag{15}$$

where E is the Green strain.
For time integration, the generalized-α [31] method has been chosen. Thus, the linear system obtained in Eq. (12) is solved using a Preconditionned Conjugate Gradient (PCG). This results in a new displacement increment $d\mathbf{d}$ used to move the domain. The process then repeats until

$$\left\|\mathbf{\Psi}(\mathbf{d}_{\mathrm{n+1}}^{i+1})\right\|_{\infty} \leq \varepsilon_{newton} \tag{16}$$

where ε_{newton} is a chosen convergence criterion.

3. Mesh movement solver

As discussed in the first section, immersed boundaries methods do not allow the precise description of geometries which is critical to accurately predict boundary layers in turbulent cases. Therefore, body fitted meshes are preferred. Besides, the FSI coupling takes place at the interface between fluid and structure, so that the fluid domain has to move according to the solid displacement. This imposes to compute a grid movement for the entire fluid domain while maintaining suitable cells quality. This is particularly challenging for cases with large deflection on unstructured grid, because the mesh has no preferential direction contrary to structured mesh. This facilitates the distribution of the deformation among cells with algebraic methods such as transfinite interpolation (TFI) [32, 33], tension spring [34] analogy or torsion spring analogy [35]. These methods are either not appropriate for unstructured meshes because it implies interpolation along mesh lines, or too expensive for large scale problems, as explained in [36].

Furthermore, to be able to reproduce numerically fluid structure interaction cases with turbulent flows, mesh movement method has to be suitable for a grid with a large number of elements and different mesh size variation, especially for LES which requires fine grid resolution. However, precision of spatial schemes suffers from mesh distortion [37], so that it is preferable to avoid to deform the mesh in regions where strong velocity gradients occur. Thus, mesh movement requires an algorithm that can be fully parallelized and allowing to control which regions of the domain will withstand the deformation. For this work, a pseudo-solid method has then be developed [38, 39].

3.1. Pseudo-solid method

The goal of this method is then to define mesh deformation field in the ALE approach. The principle is to consider the fluid domain as a linear elastic solid. The new nodes position is then computed as the equilibrium position of this "pseudo" solid material. In this context, inertial effects are not advisable here so time dependencies are ignored. The mesh movement consists then in solving a linear static problem, and the displacement constrains that the domain undergo become usual boundaries conditions of a solid with imposed displacement. With a finite element formulation, it gives

$$\mathbf{K}\mathbf{d} = \mathbf{f}\,, \tag{17}$$

with $\mathbf{K}$ the stiffness matrix, $\mathbf{d}$ the nodes displacement and $\mathbf{f}$ the forces including only the displacement conditions. With this formulation, the equilibrium position of the pseudo-solid is considered to be the mesh configuration at $t = t_0 = 0$.

As explained above, it is very useful to select regions of the domain that will move without cell deformation, and the zone that will withstand the deformation. The pseudo-solid method is very convenient for this purpose because it only requires to change the element pseudo-Young modulus E, that will directly affect the cell flexibility. In fact, for an heterogeneous solid, the part that will deform first is the less rigid one. Moreover, in most of cases, the smallest cells are regrouped close to the flexible body because it corresponds to the zone of interest, and it is essential to maintain the quality of these cells. Therefore, the generic technique developed here to compute the pseudo-Young modulus field of the pseudo-solid consists in establishing a E profile as a function of the distance from the object R.

In this study, this distance R is computed with a geometrical method for unstructured simplicial meshes [40]. The pseudo-Poisson ratio of all elements is 0.2 and their pseudo-Young modulus E is computed as

$$\begin{cases} E(R < R_{min}) = 100E_{int} & \text{(18a)} \\ E(R_{min} \leq R \leq R_{max}) = E_{int} - \dfrac{(R - R_{min})(E_{int} - E_{min})}{R_{max} - R_{min}} & \text{(18b)} \\ E(R > R_{max}) = E_{min} & \text{(18c)} \\ E_{int} = E_{min} y_r & \text{(18d)} \end{cases}$$

where the pseudo-Young modulus ratio y_r, R_{min} and R_{max} are user's parameters. On the other hand, the value of E_{min} has no influence since it is a linear

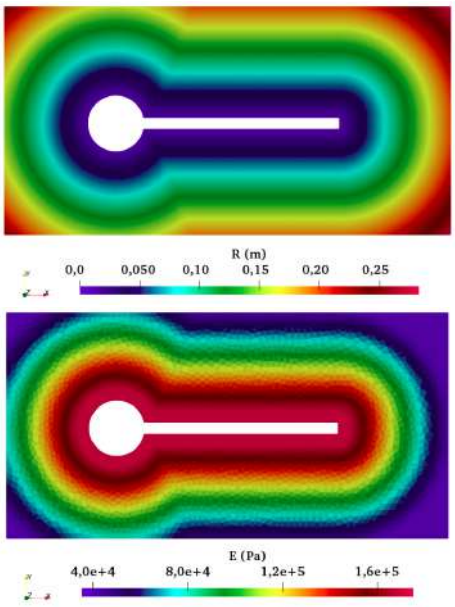

Figure 1: From top to bottom: distance field from the object R and pseudo-Young modulus field E.

elastic problem. This method ensures that for $R < R_{min}$, cells are not deformed and only move according to the imposed displacement, thanks to the high jump of E at R_{min}. On the contrary, the mesh deformation takes place in the transition zone between R_{min} and R_{max}. The size of the regions can be easily adapted for the different cases with these two parameters. However the deformation is not uniform in the transition zone, because for $y_r = 1$, only cells at $R = R_{min}$ are deformed, and for high value of y_r, most of the deformation will be taken by cells at $R \approx R_{max}$. The suitable value for y_r then depends on the size of the transition zone, the displacement amplitude and the cells size distribution. An example of both R and E fields can be visualized in Fig. 1, where the geometry used corresponds to the case presented in section 5.

This method has proven to be efficient but could be improved; the cells quality of the elements with the lowest E frequently dropped indeed first, but the deformation did not sufficiently affect cells closer to the object so that the computations stopped and failed even though cells at $R_{min} \leq R \leq R_{max}$ were still nearly non deformed.

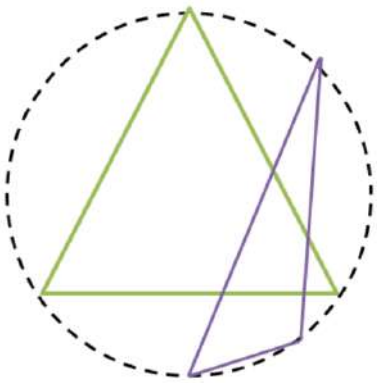

Figure 2: Representation in 2D case of a cell (in purple) and of its reference shape (in green).

3.2. Adjustment of pseudo-material properties

In order to improve the previous method, the idea is to make the cells pseudo-Young modulus E depend on their quality. The latter can be determined quantitatively by computing the cells skewness S defined by

$$S = \frac{V_{ref} - V}{V_{ref}} \tag{19}$$

where V is the cell volume and V_{ref} is the volume of the equilateral tetrahedron in 3D (or triangle in 2D), which fits in the same circumsphere as the one of the element (Fig. 2).

This criterion is then used to adjust the pseudo-solid elements flexibility during the simulation such as

$$E(t_{\mathrm{n}+1}, S(t_{\mathrm{n}})) = \frac{\left[E_{int} - E(t_0)\right]\left[S(t_{\mathrm{n}}) - S(t_0)\right]}{S_{max} - S(t_0)} + E(t_0). \tag{20}$$

where S_{max} is chosen at 0.90. Note that the pseudo-Young modulus at the beginning of the computation $E(t_0)$ is established according to the Eq. (18). Equation (20) is applied only for cells where $R > R_{min}$ because the properties of cells close to the object have to be as homogeneous as possible to guarantee that these elements are not deformed.

However, this single modification is not enough to considerably improve the method. In fact, the solving of Eq. (17) for a strong displacement will result in a mesh with a deformed cells zone. That will induce an increase of the pseudo-Young modulus of these cells (Eq. (19)), so that they will become more rigid

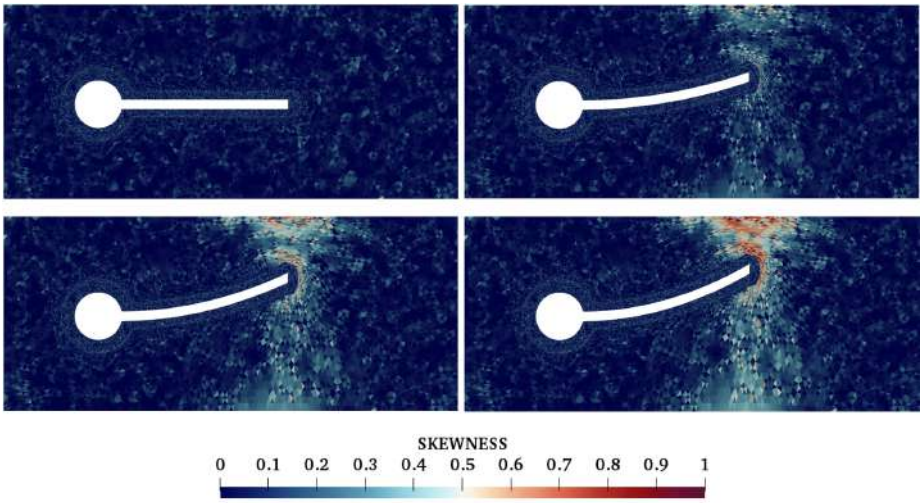

Figure 3: Skewness field of a test case with imposed displacement for the moving boundary at different instants.

than their neighbours. The solving at the next time step will then lead to a mesh where that same zone has not been deformed because of the previously computed high value of E, but their neighbours on the contrary will withstand all the deformation. The issue here is that the solved problem is still defined according to the initial configuration, and therefore the cell skewness S cannot evolve progressively. To make this technique efficient, the reference configuration used to compute the stiffness matrix $\mathbf{K}$ has to be updated at each time step with the new node position, which means to update continuously the equilibrium position of the pseudo-solid. The computed displacement becomes then an increment $d\mathbf{d}_{n+1}$ used to move nodes between their position at t_n and the new one at t_{n+1}.

An example of application of the full method is given in Fig. 3. It shows skewness fields of a test case where a domain boundary, the rod behind the cylinder, moves according an imposed sinusoidal displacement at different moments.

For this test, a mesh with inhomogeneous cell size has been used; close to the cylinder and the rod, a zone with small elements can be identified. The mesh movement strategy has to ensure that these cells will not be too much

deformed as explained in previous section. With the present method, the good behaviour is obtained by choosing a correct value for R_{min}. The different snapshots highlight that the skewness in this region remains intact. Moreover, it can also be seen that the two critical zones in terms of skewness progressively appear; one at $R = R_{min}$ and the other at $R = R_{max}$. That can be explained by the stronger pseudo-Young modulus gradients of theses regions. Nevertheless, the two last snapshots prove that the rigidification of these cells leads to a smooth cell deformation, which results in a satisfying skewness distribution.

A comparison of the method of section 3.1 and the method of section 3.2 is given in Fig. 4. It shows that without the new formulation, only elements

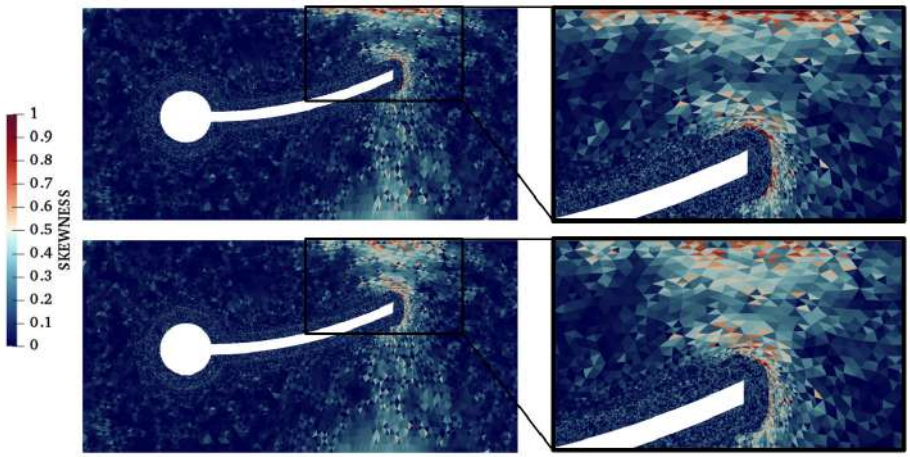

Figure 4: Comparison of the pseudo-solid method of section 3.1 (top) and the method of section 3.2 (bottom).

with low value of E tend to deform, while the other cells in the transition zone remain nearly unchanged. With the adjustment of pseudo-material elements properties, it is clear that the skewness field is much more homogeneous, thanks to the rigidification of close wall cells. This last technique appeared consequently more robust to handle strong displacement and maintain a lower maximum skewness. An example of pseudo-Young modulus after a large displacement is given in Fig. 5. It emphasizes that regions forced to stretch see their cell skewness decrease, and on the other hand compressed regions undergo growing skewness. This causes a pseudo-Young modulus profile quite different from the one at $t = 0$ given in Fig. 1.

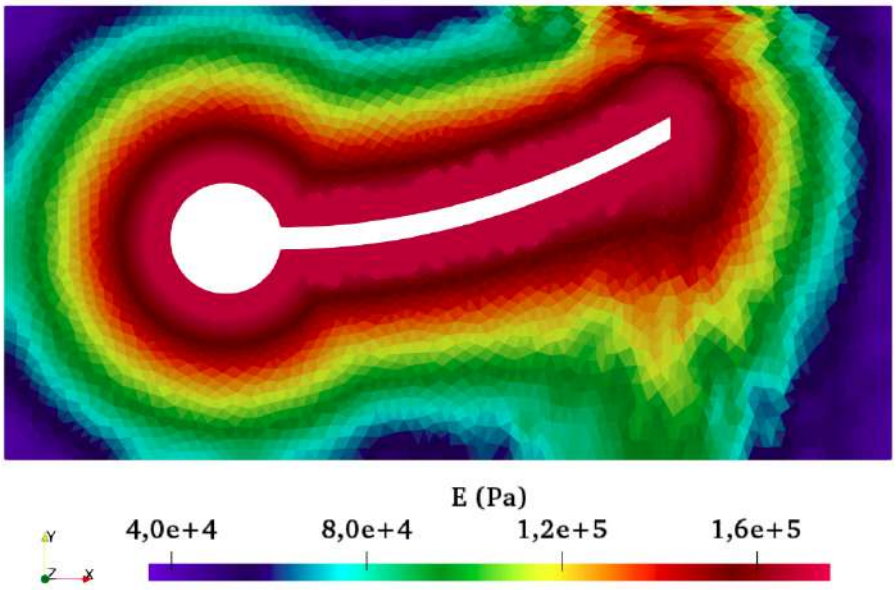

Figure 5: Pseudo-Young modulus field after large deflection of the rod while adjusting the pseudo-material properties with Eq.(20).

This efficient mesh deformation method presents then the advantage to be robust, easy to implement and without parallelization issues. Furthermore, it allows to control which mesh region can be deformed or not.

3.3. Dynamic mesh adaptation

However, for certain cases with very large deformation, moving or rotating object, mesh movement method alone cannot conserve a mesh describing the changing geometry. The only solution is then to produce a completely new mesh, adapted to the new geometry i.e to perform dynamic mesh adaption. In YALES2, the re-meshing step is based on MMG, the sequential anisotropic mesh adaptation library for tetrahedral (3D) and triangle elements (2D) [41]. The parallel mesh adaptation strategy proposed by Benard et al. [42] is applied. The benefit of DMA has already been discussed in various configurations including simulations of multiphase flows [43, 40] or moving bodies [44]. To avoid to perform the grid adaptation procedure at each time step, a criterion on the maximum allowed rate of element deformation is defined based on the

element skewness. After each time step, the mesh quality is assessed by computing the maximum skewness in the computational domain $\|S\|_\infty$. If this value exceeds a given threshold S_{lim}, the re-meshing step (grid adaptation procedure) is triggered, and all data field are interpolated on the new mesh. To combine efficiently this feature with the pseudo-material method, the stiffness matrix $\mathbf{K}$ has to be updated at each re-meshing step. In fact, a new mesh with a low maximum skewness has to be considered as a new equilibrium position. Besides, the previous E field resulting from adjusting the pseudo-Young modulus as a function of skewness becomes irrelevant because the skewness field is completely changed. The distance from the object R is then recomputed and a new pseudo-Young modulus field is established from Eq. (18). The entire method for mesh movement developed in this work is summarized in Fig. 6.

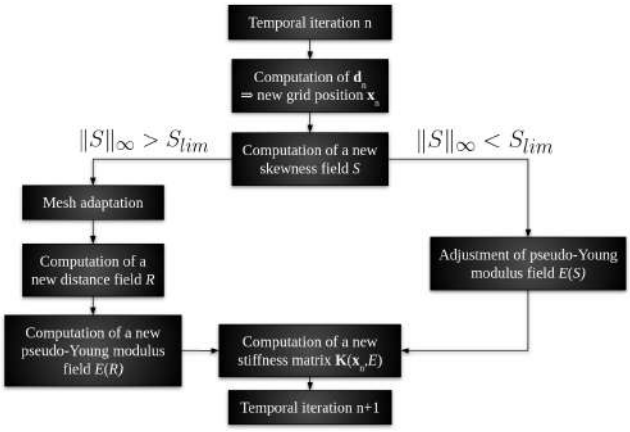

Figure 6: Scheme of the mesh movement method developed in this work.

4. FSI coupling algorithm

FSI simulations consist in coupling fluid (ALE) and solid (SMS) solvers. The coupling conditions occur at the interface Γ between fluid and solid as,

$$\begin{cases} \mathbf{u}_{n+1} = \dot{\mathbf{x}}_{n+1} = \dfrac{\mathbf{d}_{n+1} - \mathbf{d}_n}{\Delta t} & \text{(21a)} \\ \mathbf{f}_{n+1} = \displaystyle\int_\Gamma \left(\mu \frac{\partial \mathbf{u}_{n+1}}{\partial \mathrm{n}} - P_{n+1}\mathbf{n} \right) d\Gamma & \text{(21b)} \end{cases}$$

with μ the dynamic viscosity and $\mathbf{n}$ the normal direction to Γ pointing on the solid to fluid direction, with $\partial/\partial n$ the derivative with respect to this normal

vector. In fact, solid imposes its velocity to fluid while fluid applies force on solid through viscous shear and pressure. The coupling is then performed by data exchange between solvers at the interface Γ ensured by the CWIPI (Coupling With Interpolation Parallel Interface) library [45]. This library allows to compute data interpolation based on boundary nodes coordinates, which is mandatory when meshes are not coincident. It can work with two meshes composed of different element type and it also manages the parallel communications allowing to benefit of the massively parallel performance of each solver.

4.1. Coupling scheme

As explained in the introduction, the coupling approach is called partitioned coupling [8]. This choice is motivated by the flexibility of this approach to consider turbulent flows in complex geometries. Nonetheless, this method can lead to stability issues when used with a loosely coupling approach where displacements and forces are exchanged only once per time step [46]. In doing so, low density ratio ρ_s/ρ_f cases cannot be reproduced because of the well known added mass effect [47]. Therefore a strongly coupled approach is used in this work, consisting in exchanging data between solvers until convergence. This ensures the consistency of the two solutions. The FSI coupling scheme is given Fig. 7 and is similar to the one proposed by Breuer et al. [16]. This coupling scheme can be detailed into different steps:

1. The $n+1$ time iteration begins with computation of the time step value Δt_f given the stability condition of the Runge–Kutta method used by fluid solver. Note that the SMS uses the generalized-α [31] temporal scheme which is unconditionally stable. Thus, Δt_f is sent from the fluid to the solid and $\Delta t_s = \Delta t_f$ is imposed for the SMS.
2. New displacement of the interface Γ is estimated thanks to the following extrapolation

$$\mathbf{d}^0_{\mathrm{n}+1} = \mathbf{d}_{\mathrm{n}} + \alpha_0 \Delta t_f \mathbf{v}_{\mathrm{n}} + \alpha_1 \Delta t_f (\mathbf{v}_{n-1} - \mathbf{v}_{\mathrm{n}}) \tag{22}$$

   where $\mathbf{v}$ is the solid velocity, and α_i are interpolation coefficients. For $\alpha_0 = 1$ and $\alpha_1 = 0$, Eq. (22) corresponds to a linear extrapolation while for $\alpha_0 = 1$ and $\alpha_1 = 1/2$ it corresponds to a quadratic extrapolation. This last option leads to a faster convergence so it is used in this work.

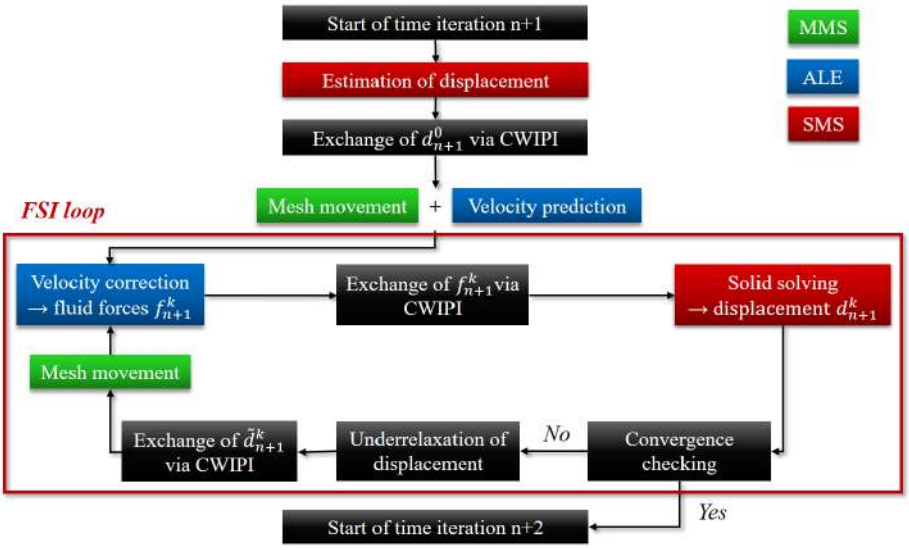

Figure 7: FSI coupling scheme used for the present work.

3. Mesh movement is solved thanks to the method explained in section 3 with the displacement condition $\mathbf{d}^0_{n+1}$. That results in a nodes velocity field $\dot{\mathbf{x}}^0_{n+1}$ used to perform the "velocity prediction" step, Eq. (4). The intermediate velocity $\mathbf{u}^*_{n+1}$ obtained is stored apart.
4. A new pressure field is then determined with Eq. (6) and used to perform the "velocity correction step" via Eq. (5). With the resulting pressure and velocity fields, the fluid force applied on the solid $\mathbf{f}^k_{n+1}$ can be computed. Here the upper index k corresponds to the number of subiterations in the FSI loop. Note that absence of this index refers to converged values of previous time step.
5. The $\mathbf{f}^k_{n+1}$ field is sent from the fluid to the solid by means of the CWIPI library.
6. The displacement $\mathbf{d}^k_{n+1}$ in the solid is computed with the methodology detailed in section 2.2.
7. At this stage, both fluid and solid have been solved at least once. The dynamic equilibrium is then checked to verify the consistency of the two solutions. This consists in checking

$$\frac{\left|\left|\mathbf{d}^k_{n+1} - \mathbf{d}^{k-1}_{n+1}\right|\right|_\infty}{\left|\left|\mathbf{d}^k_{n+1} - \mathbf{d}_n\right|\right|_\infty} \leq \varepsilon_{FSI}\,, \tag{23}$$

where ε_{FSI} is a chosen convergence criterion. If the FSI solution is converged, the solution at the considered time is finally determined and next time step can be started.

8. Otherwise, the computed displacement has to be underrelaxed on Γ with

$$\tilde{\mathbf{d}}^{k}_{\mathrm{n}+1} = \omega \mathbf{d}^{k}_{\mathrm{n}+1} + (1-\omega)\mathbf{d}^{k-1}_{\mathrm{n}+1} \tag{24}$$

where ω is a constant underrelaxation factor defined by the user. This value can also be computed at each subiteration by different means [48] but tests for our cases show that these methods did not allow to guarantee stability. Then, an accurate value of ω has to be found for the different cases; a too large value will make the computation diverge or will cause instability on fluid forces. On the other hand, the lower ω is, the greater will be the total number of subiterations N_{FSI} required before reaching convergence.

9. The underrelaxed displacement $\tilde{\mathbf{d}}^{k}_{\mathrm{n}+1}$ is then sent to the fluid via CWIPI.
10. A new field of $\dot{\mathbf{x}}^{k}_{\mathrm{n}+1}$ is computed thanks to the mesh movement solver (MMS). It has to be precised that before the solving, the domain is put back to its position at t_{n}. A new increment of displacement has to be computed but the adjustment of pseudo-material parameters with Eq. (20) has to be done only once the convergence is reached.

With the previously stored velocity prediction $\mathbf{u}^{*}_{\mathrm{n}+1}$ and the updated $\dot{\mathbf{x}}^{k}_{\mathrm{n}+1}$, new pressure and velocity fields can be determined so that step 4 can be repeated and updated fluid forces $\mathbf{f}^{k+1}_{\mathrm{n}+1}$ can be computed, closing so the FSI loop. This method thus ensures stability with a partitioned coupling and can be easily implemented, but presents the main drawback that the computational cost will depend on the number of FSI subiterations necessary to reach convergence.

The skipping of the velocity prediction once in the FSI loop was initially proposed by Fernandez et al. [49]. It allows to reduce computational cost and it has been shown that it does not affect the final result.

5. Verification in a canonical case

In order to assess the present methodology, a 2D laminar FSI test case is first considered: the benchmark proposed by Turek and Hron [50]. This numerical case consists in the interaction between an elastic rod and a laminar

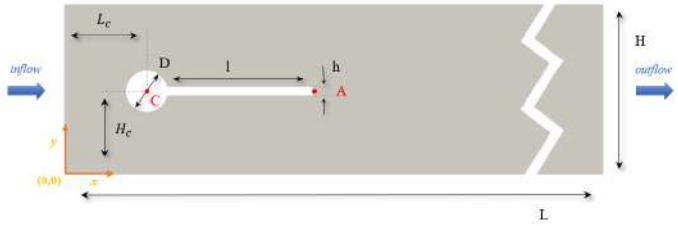

Figure 8: Sketch of the studied numerical test case.

Geometry parameters	Value [m]
Cylinder diameter	$D = 0.1$
Cylinder center x-position	$L_c = 0.2$
Cylinder center y-position	$H_c = 0.2$
Channel lenght	$L = 2.5$
Channel height	$H = 0.41$
Deformable structure length	$l = 0.35$
Deformable structure thickness	$h = 0.02$

Table 1: Dimensions of the sketch in Fig. 8.

incompressible flow. The benchmark proposes to validate each solver independently in preliminary tests. Therefore, three different test cases including mesh convergence studies are presented in this part.

5.1. Case presentation

This case is inspired by the older benchmark of an incompressible flow around a cylinder [51] except that a flexible rod is attached to the back side of the cylinder. The geometry and dimensions are given in Fig. 8 and Tab. 1. By measuring from the left bottom corner of the channel, the cylinder center position is then $C = (0.2, 0.2)$ while the rod tip is situated at $A = (0.6, 0.2)$. It should be noticed that the setup is intentionally non-symmetric (with $H_c \neq H/2$) to prevent any influence of the computation precision. For the three following tests, results of the present study will be compared with results of previous simulations extracted from [50, 52]. In particular results will be compared with the simulations performed by Turek and Hron [50], who initially proposed this benchmark.

	$M1_f$	$M2_f$	$M3_f$	Turek and Hron [50]
Δx_1 [m]	1×10^{-3}	8×10^{-4}	6×10^{-4}	N.A.
Δx_2 [m]	1.25×10^{-2}	1×10^{-2}	0.75×10^{-2}	N.A.
N_{elem} ($\times 10^3$)	73	98	173	37

Table 2: Characteristics of the three meshes used for CFD3.

Their simulations are performed based on a fully implicit monolithic ALE-FEM method with a fully coupled multigrid solver [12].

5.2. CFD tests

To first validate the fluid solver alone, the benchmark proposes three cases with different physical parameters: the case named CFD3 is chosen here. The solid is considered perfectly rigid so that the test case focuses on the laminar flow description around the cylinder and the attached rod. Quantities used for comparison will then be the fluid forces applied on the whole submerged body, computed according Eq. (21b), for a fully developed flow and for one full period of the oscillation. For this case, a non stationary regime is reached where pressure distribution fluctuates.

The flow is considered as incompressible, with a density $\rho_f = 1000$ kg/m^3 and a kinematic viscosity of $\nu_f = 0.001$ m^2/s. A parabolic velocity profile $u(x = 0, y)$ is prescribed at the inlet as

$$u(x = 0, y) = 1.5 u_\infty \frac{y(H - y)}{(H/2)^2} \,. \tag{25}$$

In CFD3 case, $u_\infty = 2$ m/s leading to a Reynolds number $Re = 200$ which leads to vortex shedding behind the cylinder, as illustrated in Fig. 9. No-slip boundary conditions are applied at channel walls and at the body.

Simulations are performed on three different meshes, $M1_f$, $M2_f$ and $M3_f$ composed by triangles. They are characterized by two metric values, Δx_1 and Δx_2, which correspond to cell size close to the cylinder and the rod, and to the cell size in the rest of the domain, respectively. Theses values are given in Tab. 2.

The timestep Δt used here is computed following the Courant-Friedrichs-Levy (CFL) convective time step constraint by keeping CFL number smaller than 0.8. This leads to a time step value around 139 μs, 113 μs and 84 μs

	Mean Drag [N]	Amp. Drag [N]	Mean Lift [N]	Amp. Lift [N]	f [Hz]
Turek and Hron [50]	439.45	5.6183	-11.893	437.81	4.3956
$M1_f$	433.69	6.4297	-7.0625	485.57	4.4326
$M2_f$	435.35	6.3794	-7.4314	478.94	4.4347
$M3_f$	435.01	6.0761	-10.505	462.78	4.4373

Table 3: Results of the CFD3 benchmark proposed by Turek and Hron [50].

for meshes $M1_f$, $M2_f$ and $M3_f$, respectively. Note that these time steps are significantly smaller than in [50], where $\Delta t = 0.01$ s and $\Delta t = 0.005$ s have been tested.

As precise above, oscillating fluid forces are compared here. Amplitudes, mean value and frequencies have been computed for each mesh and are presented in Tab. 3. The results appear in agreement with the simulations performed by Turek and Hron [50]. The discrepancies on the results can probably be explained by the difference between both simulation set-up. The CSM solver is now considered in next section.

5.3. CSM tests

The solid solver needs now to be validated with pure structural test. This test consists in computing the deformation of the flexible rod in a gravitational field $g = (0, 2)$ m/s^2 without taking into account the fluid. In this study, the CSM3 test is chosen because it is the only time dependant case. It starts from the undeformed configuration and as there is no damping, the structure immediately oscillates periodically. The material is characterized by a Poisson's ratio of $\nu_s = 0.4$, a Young modulus of $E = 1.4$ MPa and a density of $\rho_s = 1000$ kg/m^3. As significant deformations are expected, the Saint-Venant-Kirchhoff material model is used.

Three meshes have been made for this test, corresponding only to the deformable part of the body because the cylinder is always considered perfectly rigid. These meshes are only composed by 9-nodes quadrilaterals of size Δx given in Tab. 4.

As the structure is clamped to the backside of the cylinder, a non displacement boundary condition is applied to the corresponding nodes. The chosen

	$M1_s$	$M2_s$	$M3_s$	Turek and Hron[50]
Δx [m]	4×10^{-2}	2×10^{-2}	1×10^{-2}	N.A.
N_{elem}	9	18	70	5120

Table 4: Characteristics of the three meshes used for CSM3.

	Mean d_x [mm]	Amp. d_x [mm]	Mean d_y [mm]	Amp. d_y [mm]	f [Hz]
Turek and Hron [50]	-14.305	14.305	-63.607	65.160	1.0995
$M1_s$	-14.057	14.057	-63.367	63.367	1.1074
$M2_s$	-14.398	14.394	-64.113	64.436	1.1053
$M3_s$	-14.257	14.452	-64.163	64.872	1.0972

Table 5: Results of the CSM3 benchmark proposed by Turek and Hron [50].

time step is $\Delta t = 0.005$ s (same than in [50]) and is applied with the generalized-α method with the spectral radius $\rho_\infty = 0.8$.

For comparison, displacement of previously defined point A is tracked in time. Once again, mean values, amplitudes and frequencies are computed for displacements d_x and d_y along x-axis and y-axis, respectively. All results are gathered in Tab. 5.

Differences with Turek and Hron results [50] are here minor, even though grid used in the reference study is much finer (5120 elements). Efficiency of 9-nodes quadrilaterals seems here confirmed. This close agreement allows then to successfully validate the CSM solver.

5.4. FSI tests

Finally, to validate the coupling between fluid and solid solvers, the FSI3 benchmark has been reproduced. The fluid forces are now applied to the flexible structure so that it deforms and starts interacting with the flow. Fluid properties are the same as in CFD3 but for the solid, the Young modulus is chosen as $E =$ 5.6 MPa. This case is particularly challenging because $\rho_f = \rho_s = 1000$ kg/m^3, which maximizes the importance of the added-mass effect. Besides, the channel is narrow compared to the expected structure deflections; that imposes a very efficient mesh movement algorithm to keep a low maximum skewness. The method presented in section 3 is used here with $R_{min} = 0.02$ m, $R_{max} = 0.2$ m

	Mean d_x [mm]	Amp. d_x [mm]	f d_x [Hz]	Mean d_y [mm]	Amp. d_y [mm]	f d_y [Hz]
min and max from [50, 52]	-3.04 / -2.48	2.53 / 2.87	10.1 / 11.63	1.27 / 1.55	34.38 / 36.63	4.98 / 5.5
$M1_f$&$M1_s$	-3.08	2.86	11.1	1.41	36.22	5.53
$M2_f$&$M2_s$	-3.06	2.82	11.02	1.30	36.16	5.51
$M3_f$&$M3_s$	-3.01	2.77	10.99	1.42	35.89	5.49

Table 6: Results of the FSI3 benchmark proposed by Turek and Hron [50]. Minimum and maximum values of previous simulations extracted in Ref. [50, 52] are given for comparison.

and $y_r = 100$. These values allow the most refined zone close to the body to remain intact while coarser regions close to the channel walls will withstand the deformation. That can be seen in Fig. 9 which shows the resulting grid $M1_f$ when the rod is at the maximum deflection. The method ensures a good grid quality without needs of dynamic mesh adaptation step. Concerning the FSI coupling, the convergence criterion defined in Eq. (23) is set at $\varepsilon_{FSI} = 1 \times 10^{-5}$ and the underrelaxation factor is $\omega = 0.1$. Because of the density ratio $\rho_s/\rho_f = 1$, higher values of ω do not allow to reach convergence inside the FSI loop. Nonetheless, it results in a relatively low mean number of subiterations N_{FSI} of 15.04 while this number averaged 55.21 in [16] for the same value of ω. However, Breuer et al. [16] managed to reach convergence with $\omega = 0.5$ and $N_{FSI} = 9.38$ which was not possible in the present study.

In the original case, the authors propose to progressively establish the flow starting with a zero velocity field in all the domain. Note that this cannot be done with the present algorithm because the fluid forces were so low that the importance of the added mass effect was relatively too important. Such an unstable configuration surely requires a more stable monolithic approach. Therefore, the coupling has here been started with a fully developed flow, as computed in CFD3 case.

Figure 9 also depicts an instantaneous velocity field. The vortex shedding at the cylinder is clearly visible and induces oscillating forces applied in the entire body as it has been seen in the CFD3 case of section 5.2. Theses forces cause the flexible structure displacement resulting in periodic displacement of the rod behind the cylinder.

For comparison, sinusoidal displacement of previously defined point A are measured and presented in Fig. 10 and in Tab. 6. Even if numerical methodolo-

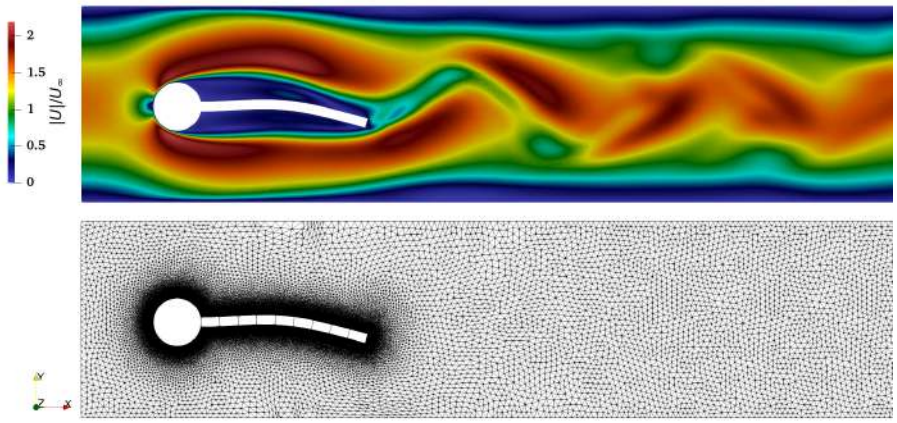

Figure 9: Velocity field and deformed mesh of FSI3 benchmark reproduced with $M1_f$ & $\mathrm{M1}_s$. Note that the domain has been cropped on the right side to focus on the deformable part.

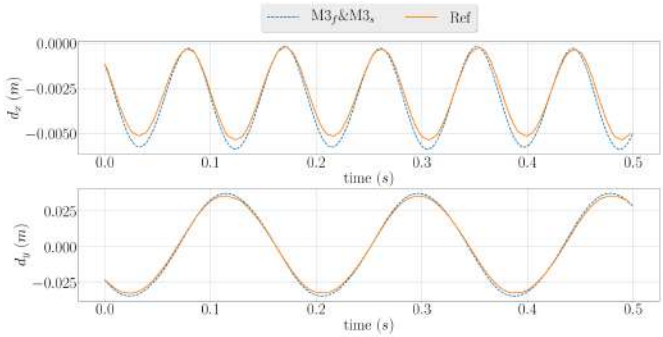

Figure 10: Displacement of point A along x-axis (top) and y-axis (bottom) obtained with $\mathrm{M3}_f$&$\mathrm{M3}_s$ and results of the reference study [50].

gies between the present study and the work of Turek and Hron [50] are different, the results appear in agreement. Note that for this case, a comparison of results obtained by 7 other groups have been reported in [52], including a variety of numerical methods. For each quantities, the minimum and maximum values are reported in Tab. 6. Given the complexity of the present case, a spreading of the tip displacement prediction can be noticed, and the results of the present study appear in agreement with these previous simulations. Consequently the overall agreement with reference data enables to validate the present FSI solver.

Another proposed benchmark FSI2 [50] has also been reproduced and satisfying results have been obtained. In this test case, $\rho_s/\rho_f = 10$ which makes the coupling less unstable. This allows to apply an underrelaxation of $\omega = 0.3$ and convergence is reached with a number of FSI subiterations that averages 4.5. Contrary to the FSI3 case, here the larger deflections impose the use of the dynamic mesh adaptation. Results of this case can be visualized in the supplementary material.

6. Validation on a realistic complex case

For completeness, the FSI solver is now validated on the experimental case performed by Kalmbach et al. [53], named FSI-PfS-2a. This case deals with a turbulent flow which leads to large deformation of the structure.

6.1. Case presentation

This test case is derived from the 2D case considered in the previous section; it consists of a cylinder fixed in a water channel. A flexible rubber structure with an attached steel weight is clamped behind it. The geometry and dimensions are detailed in Fig. 11 and Tab. 7.

The inflow velocity u_{inflow} is set at 1.385 m/s which gave experimentally nearly symmetrical, large and reproducible structural displacement. The measured inflow turbulence level is $Tu_{inflow} = 0.02$ and is considered sufficiently low to be ignored in the rest of the study, a choice motivated by previous studies which also did not take it into account [54, 55]. The water density is $\rho_f = 1000$ kg/m^3 and the dynamic viscosity is $\mu_f = 0.001$ Pas. The structure is composed of two different materials; the flexible part was made with para-rubber while the bonded rear mass is made of steel. All properties can be found

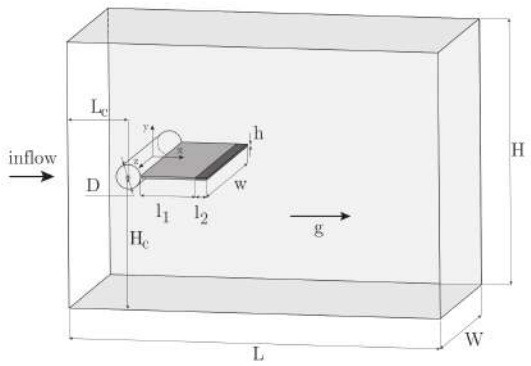

Figure 11: Sketch of the studied experimental test case. Extracted from [53].

Geometry parameters	Value [m]
Cylinder diameter	$D = 0.022$
Cylinder center x-position	$L_c = 0.077$
Cylinder center y-position	$H_c = 0.120$
Test section lenght	$L = 0.338$
Test section height	$H = 0.240$
Test section width	$W = 0.180$
Deformable structure length	$l_1 = 0.050$
Deformable structure height	$h = 0.002$
Deformable structure width	$w = 0.177$
Rear mass length	$l_2 = 0.010$
Rear mass height	$h = 0.002$
Rear mass width	$w = 0.177$

Table 7: Dimensions of the sketch in Fig. 11.

in Tab. 8. The rear mass is here added to emphasize the structure motion and trigger the second swiveling mode, unlike the first case FSI-PfS-1a [54].

	Density [kg/m3]	Young's modulus [MPa]	Poisson's ratio
Flexible structure (para-rubber)	1090	4.1	0.48
Rear mass (steel)	7850	2.1×10^5	0.3

Table 8: Structure properties for the FSI-PfS-2a case.

The Reynolds number based on cylinder diameter gives $Re = 30\,470$ and it is observed experimentally that the flow is in a sub-critical regime. The boundary layers around the cylinder are still laminar but the flow becomes turbulent downstream. At this point, a large variety of spatial and temporal frequencies appears but only the lowest ones can be found in the structure displacement. The flexible part thus deforms in the second swiveling mode with a frequency of $f_{FSI} = 11.25$ Hz.

6.2. Numerical setup

In order to reduce computational cost, a subset case had been used in [54] where dimensions along z-axis were reduced. Structure width then became $w' = l_1 + l_2$, and the gap between channel walls and the structure was ignored so that the test section width W' was equal to w'. For the full case, these walls were assumed slip while periodic boundary conditions were used for the subset case. Results comparison in terms of structure deflection but also flow field between the two cases concluded that this simplification was valid. Only the subset case is then considered in the present study with the difference that the small gap between flexible part and channel walls was considered. Test section height then becomes $W' = l_1 + l_2 + (W - w)$. Therefore, solid nodes on these sides are free and a boundary condition that imposes a zero z-displacement is not mandatory. For the fluid, slip walls are assumed for these boundaries to maintain the blocking effect and limit flow recirculating and thus reproduce the same effect than in the experimental setup.

Considering that the flow relatively far from the body will not affect the structure motion, fluid mesh has been refined in the zone of influence around the cylinder and the plate. First cell size close to the body is equal to $9 \times 10^{-3} D$ and slowly decreases to $2.3 \times 10^{-2} D$ in the rest of this region, as it can be seen in Fig. 12. Consequently, a grid composed of about 40 million tetrahedra is generated. As precised above, all channel walls are considered slip because the

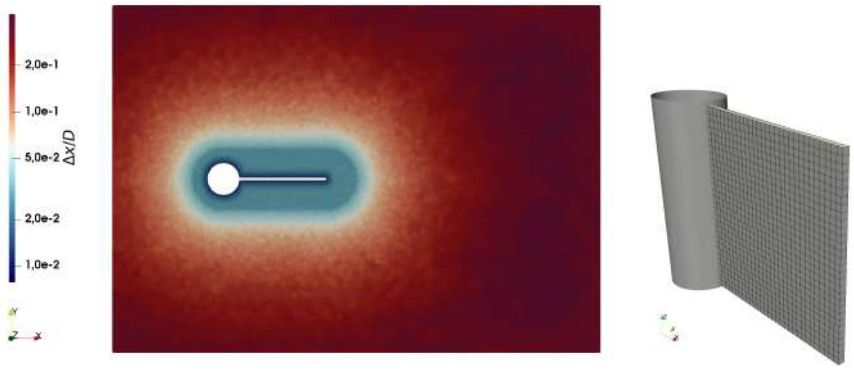

Figure 12: Fluid mesh metric field (log scale)(left) and solid mesh (right) used to reproduce the FSI-PfS-2a case.

full resolution of their boundary layers would be too costly. On the other hand, the cylinder and the structure are defined as no-slip walls. Once again, the timestep of the simulation is based on the CFL condition leading to $\Delta t \approx 5 \times 10^{-5}$ s. For the flow simulation, LES is performed and the SGS model used here is the dynamic Smagorinsky model [56]. The pseudo-solid mesh movement is used with $R_{min} = 0.0025$ m, $R_{max} = 0.08$ m and $y_r = 100$ and is combined with dynamic mesh adaptation.

Thanks to CWIPI (section 4), the two meshes do not need to be coincident. Thus, the solid mesh is composed by 900 27-nodes hexahedrons of size equal to structure height h and can be visualized in Fig. 12. The nodes against the cylinder are fixed but all the other ones are free to move, building five solid faces coupled with the fluid. For temporal advancement, the generalized-α method is used with a spectral radius $\rho_\infty = 1.0$. In a similar manner than in [55], no structural damping are applied.

As explained in the previous section, the flow is first established before starting the FSI coupling. The underrelaxation factor is $\omega = 0.2$ and the FSI convergence criterion ε_{FSI} is equal to 5×10^{-4}. It results in a mean number of

subiterations $N_{FSI} = 22.6$. A cluster specifically designed for memory bound applications (eg: CFD codes such as YALES2) was used. It is based on AMD Epyc 7302 processors with 16 cores and 128Mo of L3 cache, providing high memory bandwidth for each cores. Nodes with 128GB of RAM and two processors are connected with an InfiniBand HDR100 network (100Gb/s). The computation of the FSI-PfS-2a case was carried out on 240 cores for the fluid and 16 cores for the solid, so that one physical second could be predicted in 519 hours wall-clock, i.e 133kH.CPU.

6.3. Results

A visualization of the resulting simulation is given Fig. 13 and an animation is available in the supplementary material. It shows that even if the structure displacement is mainly two dimensional, three-dimensional flow structures appear in the wake of the cylinder. Furthermore, the velocity and vorticity fields shown in Fig. 14 highlight the fact that the structure motion can deviate the vortex trajectories.

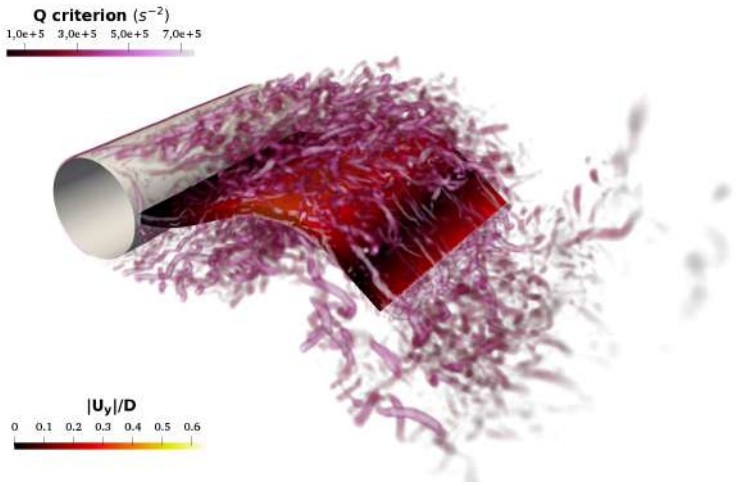

Figure 13: Visualization of the Q-criterion for the FSI-PfS-2a case. Structure is colored by the normalized y-displacement.

In order to compare with experimental data, a probe is positioned on the solid at 2 mm from the plate tip. To verify if the displacement can be considered uniform along the z-axis, normalized y-displacement d_y/D is measured at plate

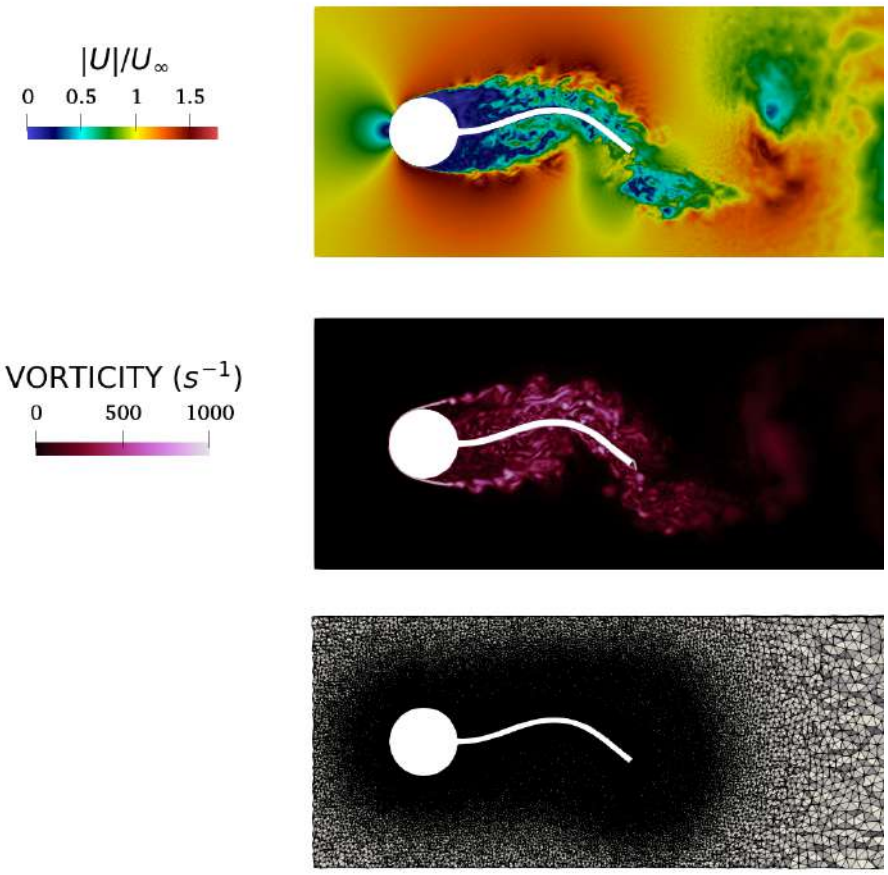

Figure 14: Visualization of the normalized velocity field, vorticity field and deformed mesh (from top to bottom) for the FSI-PfS-2a case. Note that the fields have been cropped, entire domain can be seen in Fig. 12.

center $z = 0.0$ and extremities $z \pm 0.03$. The time evolution of these quantities is plotted in Fig. 15. It can be seen that deviation between the three results

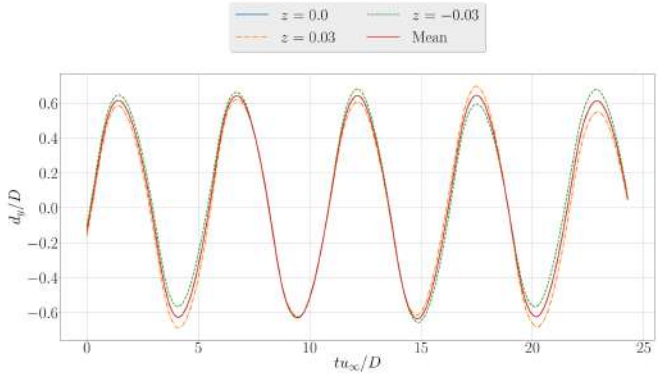

Figure 15: Normalized y-displacement at different z locations.

is minor, confirming that d_y/D can be computed as a mean value of this three points. This mean value is then averaged in 23 sub-parts of the phase in order to compare with experimental data. Results are accumulated on 5 periods leading to a mean standard deviation of about 0.01. The two phase-averaged d_y/D signals are shown in Fig. 16 where standard deviation of each point is also represented. This figure highlights the good agreement between the numerical

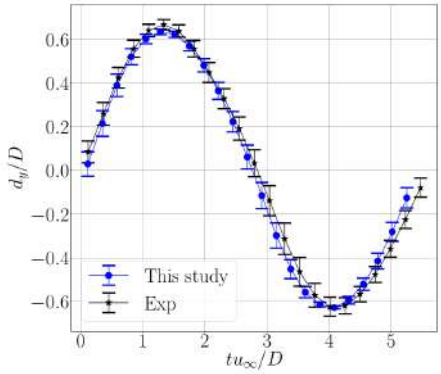

Figure 16: Comparison of the numerical and experimental averaged phase of normalized y-displacement.

results and the experimental data. Table 9 gathers the maximum, minimum,

	$d_y/D\|_{max}$	$d_y/D\|_{min}$	Mean d_y/D	Amp. d_y/D	f d_y/D [Hz]
Exp	0.667	-0.629	0.019	0.648	11.25
This study	0.632 (5.27%)	-0.627 (0.37%)	0.002 (86.37%)	0.629 (2.89%)	11.73 (4.23%)

Table 9: Numerical results and comparison with the experiment.

amplitudes, mean value and frequency of the normalized y-displacement.

The asymmetries of experimental data are unexpected considering the symmetry of the entire setup, but may be explained in [55]. After careful analysis, it was concluded that errors were related with the assembly of the structure, especially the bond between the rubber plate and the cylinder and the bond between the cylinder and the test section. That explains the undesired mean value of d_y/D of 0.019 while no mean displacement is expected in this direction due to symmetry. This experimental issue makes the precise comparison with the reference value for $d_y/D|_{max}$ and $d_y/D|_{min}$ irrelevant, but the amplitude of the structure oscillation is still valid and the numerical result deviates only of about 2.9%. This is also true for the predicted frequency where the error is around 4.2%. The overall agreement with experimental values confirms that the present FSI solver is able to predict turbulent case with large deformation with high fidelity.

7. Application case: simulation of a chordwise flexible pitching foil

In order to illustrate the potential of the FSI solver for its intended use, a simulation of an experimental case involving a chordwise foil is finally presented. More details can be found in [57].

7.1. Case presentation

The case is inspired by the experimental work of Hoerner et al. [6] to show how hyperflexible foils effectively adapt dynamically their shape and passively control the flow through deformation. The case consist to a pitched hydrofoil surrounded by a water stream. The experimental case with the largest foil deformation has been retained in this work. In this case, the hydrofoil has a symmetric NACA0018 geometry with a chord equal to 66 mm. It is composed

by a milled aluminum pieces reach up to the first quarter of the chord, whereas a carbon fiber with a thickness of 0.3 mm is embedded in this part and the rest of the trail is composed by silicone embodiment. The imposed pitching leads a variation in time of the angle of attack, α, as,

$$\alpha = \arctan\left(\frac{\sin(2\pi f t)}{\lambda + \cos(2\pi f t)}\right), \tag{26}$$

with $f = 2.63$ Hz the frequency, $\lambda = 2$, and t the time. The rotation axis of the foil is located at first quarter of the chord. Finally, the inflow velocity, $u_\infty = 3.07$ m.s^{-1}, leads to a chord-based Reynolds number equals to $202,620$. From experiments measure of foil deformation and left and drag force measured on the foil are available. The deformation is characterized by the angle of deformation β is defined in Fig 17. Therefore, for the rigid foil, it gives $\alpha = \beta$.

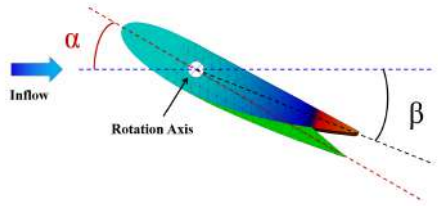

Figure 17: Definition of the angle of deformation β.

7.2. Numerical setup

The numerical configuration stays close to the experimental setup. However, some simplifications have been performed to reduce the computational cost. Concerning the geometry, the channel width is reduced from $2.65C$ to $1C$. Preliminary tests have indeed shown that this change has not affected significantly the fluid forces per unit of length. Also, the gap between the extremity of the foil and the channel wall is not taken into account, and the channel walls are considered slip to avoid strong mesh constraint to capture boundary layers at the channel wall. No-slip boundary condition is applied on the foil. Finally the gravity is taken into account and water is considered with a density $\rho_f = 1000$ kg.m^{-3} and a dynamic viscosity $\mu_f = 0.001$ Pa s. A flexible and a rigid foil cases are considered. From preliminary study a fluid mesh composed by 27 millions of tetrahedrons is used.

For the flexible foil, the first quarter of the chord (the part in aluminum) is considered as a perfectly rigid solid. The computational domain for the structural mechanics solver (SMS) is then reduced to the silicone and carbon parts, and displacement was set on the solid face which is in contact with the aluminium part. Moreover, the differences in Young modulus values between the silicone and the 0.3 mm carbone part induce high condition number of the SMS linear system. An "artificial" single material has been preferred to reduce computational cost.It has been measured that this simplification made the computation 29 times faster. From tests, the Young modulus was chosen as $E = 1.28$ MPa, the density as $\rho = 1250$ kg.m^{-3}. The poisson ratio was set to zero to prevent foil distension in spanwise direction. Finally, a mesh composed by 1900 10-nodes tetrahedrons is used.

As regards the FSI coupling, the underrelaxation factor is $\omega = 0.5$ and the FSI convergence criterion ε_{FSI} is equal to 5×10^{-4}. Moreover, in order to stabilize the FSI coupling and reduce the number of subiterations N_{FSI} required, structural damping is added. It finally results in a mean number of subiterations $N_{FSI} = 3.39$. The cluster presented in section 6.2 was also used, but this time with 20 cores for the solid and 225 for the fluid, so that one period of foil oscillation could be predicted in 53.25 hours wall-clock, i.e 13kH.CPU. It is only 6 times more than the computational cost of the rigid case simulated with the same fluid mesh.

7.3. Results

First, numerical results are compared with experimental data in terms of lift, drag and deformation angle β in Fig. 18. It can be seen that the results are in correct agreement with the experiment for the forces and for the foil deformation. The flow behaviour have then been well reproduced, allowing physical insights given that the solid problem simplification does not affect the flow configuration once the foil behaviour is similar. For the analysis of the FSI phenomenon, different post-processings have been done.

An animation showing the results is given in the supplementary material. At first, comparison of rigid and flexibles cases is shown by Fig. 19 with visualizations of the vorticity volume rendering for different angle of attack. The dynamic stall can clearly be seen. It causes the generation of a first vortice above the foil. This will create a low pressure region, attracting the surrounding fluid, especially fluid coming from the other side of the foil. This finally

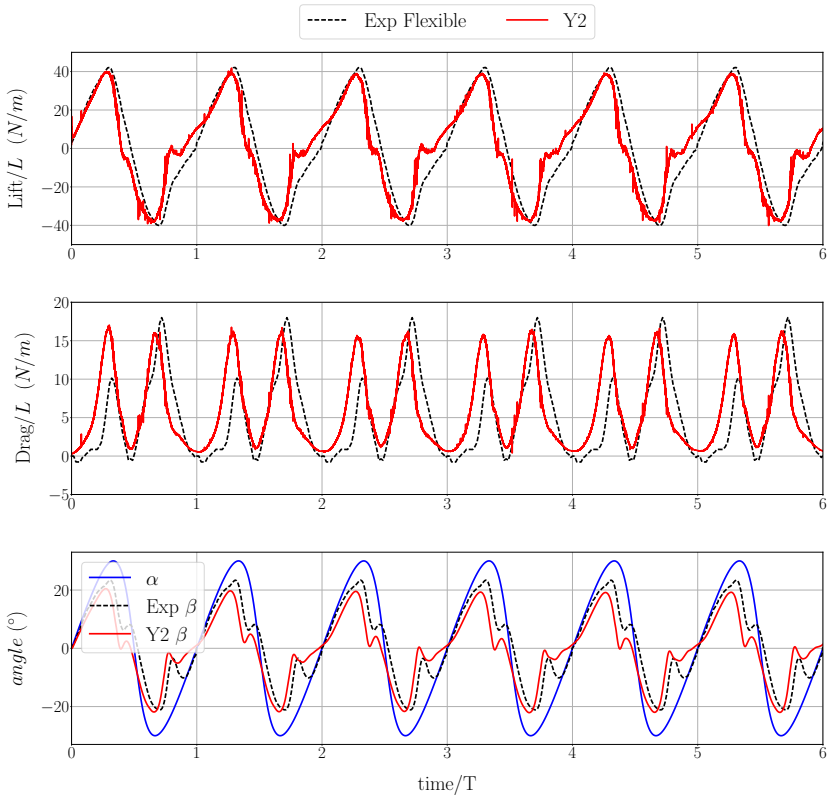

Figure 18: Comparison of forces and foil deformation with the experimental data for the flexible case.

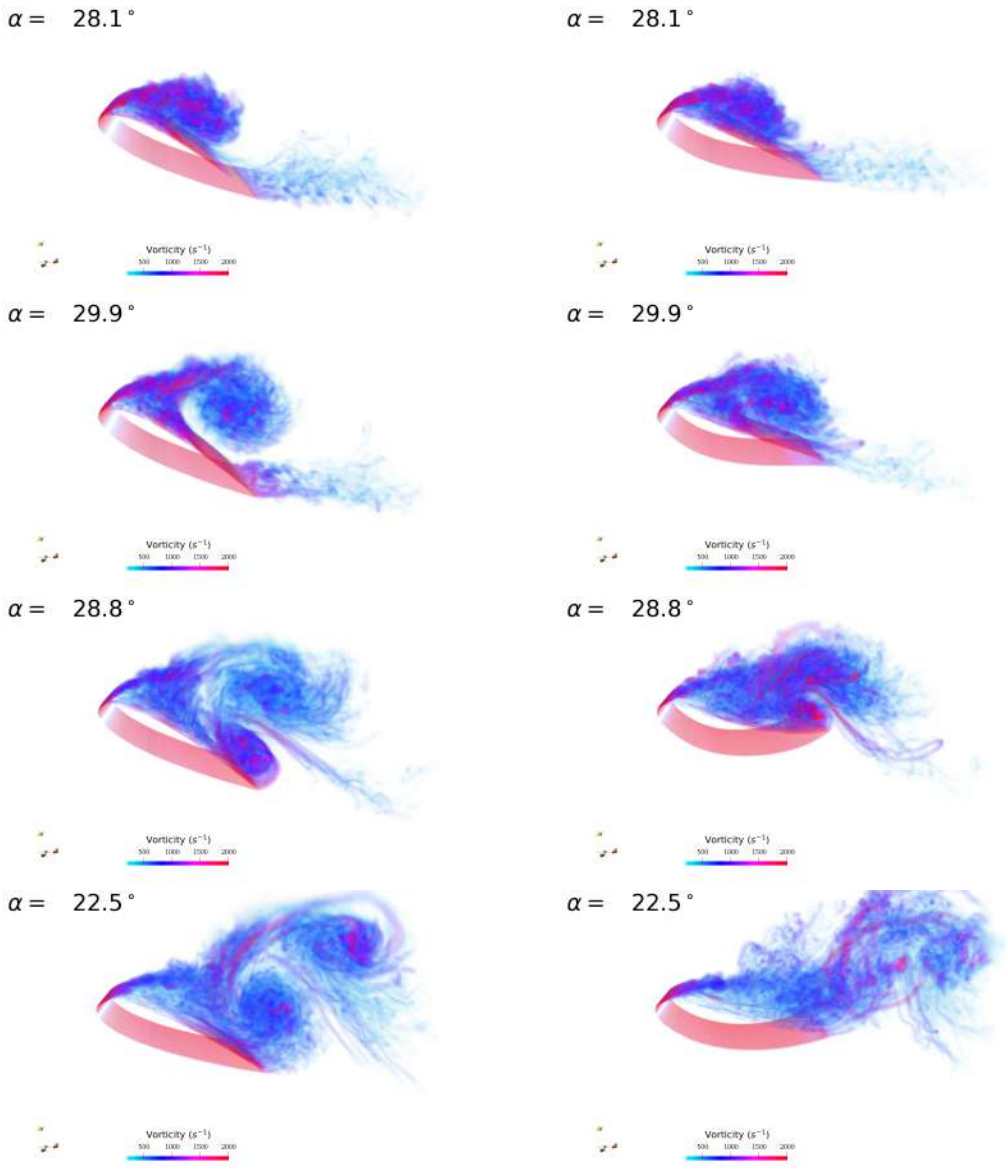

Figure 19: Vorticity volume renderings of rigid (left) and flexible (right) foil cases.

lead to the generation of a second vortice at the trailing edge. For the flexible case, the generation of this second vortice induces the foil deformation. The low pressure region appears indeed where the foil thickness is relatively small, and the pressure difference is sufficiently strong to deform significantly the foil. This finally leads to sigificantly different flow configurations between rigid and flexible cases.

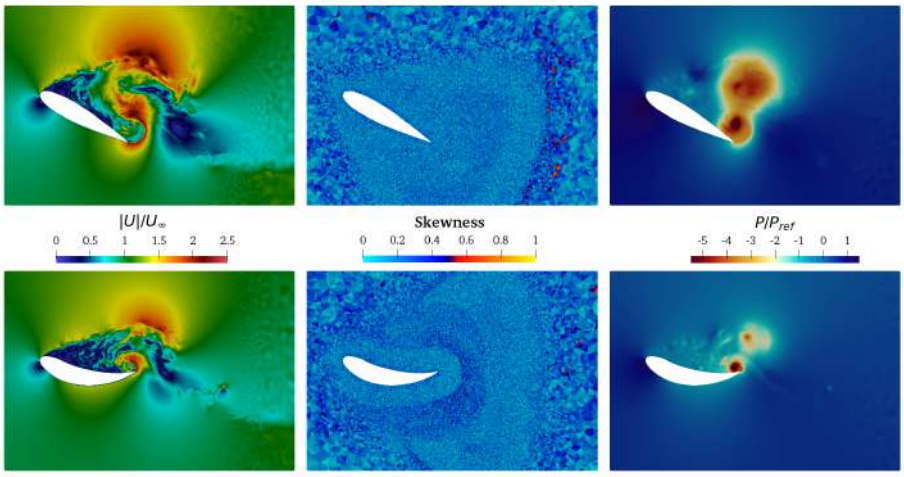

Figure 20: Velocity, skewness and pressure fields computed for the rigid (top) and the flexible (bottom) foil at $\alpha = 29.1°$.

This observation is confirmed by the analysis of the velocity and pressure fields shown in Fig. 20. The two vortices can be observed as well as the low pressure regions. The pressure distribution applied on the foil is then very different between the rigid and flexible case, explaining the differences in lift and drag measured in the experiment [6]. On this figure, the skewness fields are also shown to highlight the difference of method used for mesh movement between the two cases, given that it is more complicated to move the fluid mesh when the foil is deforming.

Foil relative displacement compared to the rigid case for an angle of attack of $\alpha = 29.1°$ is finally given in Fig. 21. It can be noticed that at the maximum deflection, deformation reaches 35% of the chord. This case then confirms that the developed FSI solver is able to reproduce cases of chordwise flexible foil with large deformation. Such simulations should lead to a better understanding of

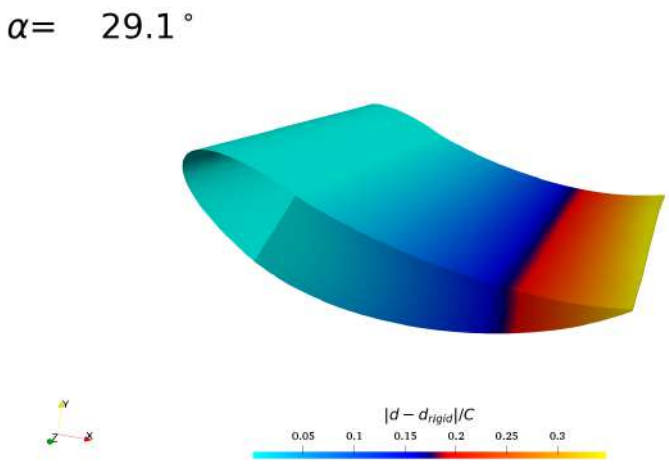

Figure 21: Relative displacement of the foil compared to the rigid case at $\alpha = 29.1°$.

the link between the dynamic stall and the flexible foil deformation in future works.

8. Conclusion

The necessity to numerically reproduce turbulent FSI case with complex geometries is growing proven by the emergence of research works involving chordwise flexible blade. These studies are promising but remain mainly experimental because the simulation of such cases with a high level of fidelity is extremely challenging. It indeed requires 3D LES to predict the dynamic stall with accuracy, and 3D solid element to handle large deformation of the structure. In this context, the present work proposes a LES-based FSI solver using 3D solid elements for the solid and unstructured grid for fluid and solid solvers. This approach aims at being universal and is based on a partitioned coupling scheme, allowing low density ratios of the structure to the fluid. For the mesh movement solving, an original pseudo-solid method has been developed and can be used with dynamic mesh adaptation strategy. This method proved to be robust and appropriate to FSI case with large deformation. The resulting FSI solver is suited for massively parallel computing and can be used without geometry restriction. Both fluid and solid solvers have been validated independently before validation of the FSI solver on a 2D laminar benchmark, including mesh

convergence study. The methodology has then been successfully applied to realistic complex case with high Reynolds number. Numerical results have shown a satisfactory agreement with the available experimental data. Finally, an experiment involving a chordwise flexible foil is successfully simulated with a 3D LES approach. This had never been reported in the literature so far and confirms the potential of the FSI solver for its intended use.

Aknowledgements

This research work has been financially supported by the french "Agence National de la Recherche" through the project DYNEOL. It was also granted access to the HPC resources of TGCC under the allocation A0092A00611 made by GENCI. The authors would like to thank Patrick Begou for his technical support, as well as Simon Mendez, Franck Nicoud and Barthelemy Thibaud for helpful discussions.

References

[1] Yuri Bazilevs, Kenji Takizawa, and Tayfun E Tezduyar. *Computational fluid-structure interaction: methods and applications*. John Wiley & Sons, 2013.

[2] Hung Truong, Thomas Engels, Dmitry Kolomenskiy, and Kai Schneider. A mass-spring fluid-structure interaction solver: Application to flexible revolving wings. *Computers & Fluids*, 200:104426, 2020.

[3] Julien Sigüenza, Desiree Pott, Simon Mendez, Simon J Sonntag, Tim AS Kaufmann, Ulrich Steinseifer, and Franck Nicoud. Fluid-structure interaction of a pulsatile flow with an aortic valve model: a combined experimental and numerical study. *International journal for numerical methods in biomedical engineering*, 34(4):e2945, 2018.

[4] Xia Wu, Xiantao Zhang, Xinliang Tian, Xin Li, and Wenyue Lu. A review on fluid dynamics of flapping foils. *Ocean Engineering*, 195:106712, 2020.

[5] Stefan Hoerner, Shokoofeh Abbaszadeh, Thierry Maître, Olivier Cleynen, and Dominique Thévenin. Characteristics of the fluid–structure interaction

within darrieus water turbines with highly flexible blades. *Journal of Fluids and Structures*, 88:13–30, 2019.

[6] Stefan Hoerner, Shokoofeh Abbaszadeh, Olivier Cleynen, Cyrille Bonamy, Thierry Maître, and Dominique Thévenin. Passive flow control mechanisms with bioinspired flexible blades in cross-flow tidal turbines. *Experiments in Fluids*, 62(5):1–14, 2021.

[7] Boyce E Griffith and Neelesh A Patankar. Immersed methods for fluid–structure interaction. *Annual review of fluid mechanics*, 52:421–448, 2020.

[8] Joris Degroote. Partitioned simulation of fluid-structure interaction. *Archives of computational methods in engineering*, 20(3):185–238, 2013.

[9] Gilberto Santo, Mathijs Peeters, Wim Van Paepegem, and Joris Degroote. Dynamic load and stress analysis of a large horizontal axis wind turbine using full scale fluid-structure interaction simulation. *Renewable energy*, 140:212–226, 2019.

[10] Toshiyuki Nakata and Hao Liu. A fluid–structure interaction model of insect flight with flexible wings. *Journal of Computational Physics*, 231(4):1822–1847, 2012.

[11] Christiane Förster, Wolfgang A Wall, and Ekkehard Ramm. Artificial added mass instabilities in sequential staggered coupling of nonlinear structures and incompressible viscous flows. *Computer methods in applied mechanics and engineering*, 196(7):1278–1293, 2007.

[12] Jaroslav Hron and Stefan Turek. A monolithic fem/multigrid solver for an ale formulation of fluid-structure interaction with applications in biomechanics. In *Fluid-structure interaction*, pages 146–170. Springer, 2006.

[13] EH Van Brummelen. Partitioned iterative solution methods for fluid–structure interaction. *International Journal for Numerical Methods in Fluids*, 65(1-3):3–27, 2011.

[14] David W MacPhee and Asfaw Beyene. Fluid–structure interaction analysis of a morphing vertical axis wind turbine. *Journal of Fluids and Structures*, 60:143–159, 2016.

[15] Ivo Marinić-Kragić, Damir Vučina, and Zoran Milas. Concept of flexible vertical-axis wind turbine with numerical simulation and shape optimization. *Energy*, 167:841–852, 2019.

[16] Michael Breuer, Guillaume De Nayer, Manuel Münsch, Thomas Gallinger, and Roland Wüchner. Fluid–structure interaction using a partitioned semi-implicit predictor–corrector coupling scheme for the application of large-eddy simulation. *Journal of Fluids and Structures*, 29:107–130, 2012.

[17] S Leonard, M Terracol, and P Sagaut. Commutation error in les with time-dependent filter width. *Computers & fluids*, 36(3):513–519, 2007.

[18] VR Moureau, OV Vasilyev, C Angelberger, and T Poinsot. Commutation errors in large eddy simulations on moving grids: Application to piston engine flows. In *Proceeding of the Summer program*, pages 157–168, 2004.

[19] Lixiang Zhang, Yakun Guo, and Wenquan Wang. Large eddy simulation of turbulent flow in a true 3d francis hydro turbine passage with dynamical fluid–structure interaction. *International journal for numerical methods in fluids*, 54(5):517–541, 2007.

[20] Silvio Tschisgale, Bastian Löhrer, Richard Meller, and Jochen Fröhlich. Large eddy simulation of the fluid–structure interaction in an abstracted aquatic canopy consisting of flexible blades. *Journal of Fluid Mechanics*, 916, 2021.

[21] Marcel Ilie. Fluid-structure interaction in turbulent flows; a cfd based aeroelastic algorithm using les. *Applied Mathematics and Computation*, 342:309–321, 2019.

[22] V. Moureau, P. Domingo, and L. Vervisch. Design of a massively parallel CFD code for complex geometries. *C.R. Mecanique*, 339(2/3):141–148, 2011.

[23] Mathias Malandain, Nicolas Maheu, and Vincent Moureau. Optimization of the deflated conjugate gradient algorithm for the solving of elliptic equations on massively parallel machines. *Journal of Computational Physics*, 238:32–47, 2013.

[24] J. Donea, A. Huerta, J.-Ph. Ponthot, and A. Rodriguez-Ferran. *Arbitrary Lagrangian–Eulerian Methods*. John Wiley & Sons, Ltd, 2004.

[25] C. Chnafa, S. Mendez, and F. Nicoud. Image-based large-eddy simulation in a realistic left heart. *Computers & Fluids*, 94:173 – 187, 2014.

[26] A.J. Chorin. Numerical solution of the navier-stokes equations. *Math. Comp.*, 22:745–762, 1968.

[27] Matthias Kraushaar. *Application of the compressible and low-Mach number approaches to Large-Eddy Simulation of turbulent flows in aero-engines*. PhD thesis, Institut National Polytechnique de Toulouse-INPT, 2011.

[28] Charbel Farhat, Philippe Geuzaine, and Céline Grandmont. The discrete geometric conservation law and the nonlinear stability of ale schemes for the solution of flow problems on moving grids. *Journal of Computational Physics*, 174(2):669–694, 2001.

[29] Daniele Boffi and Lucia Gastaldi. Stability and geometric conservation laws for ale formulations. *Computer methods in applied mechanics and engineering*, 193(42-44):4717–4739, 2004.

[30] Olek C Zienkiewicz and Robert L Taylor. *The finite element method for solid and structural mechanics*. Elsevier, 2005.

[31] Jintai Chung and GM Hulbert. A time integration algorithm for structural dynamics with improved numerical dissipation: the generalized-α method. 1993.

[32] Joe F Thompson, Zahir UA Warsi, and C Wayne Mastin. *Numerical grid generation: foundations and applications*. Elsevier North-Holland, Inc., 1985.

[33] Stephanus Petrus Spekreijse. Elliptic grid generation based on laplace equations and algebraic transformations. *Journal of Computational Physics*, 118(1):38–61, 1995.

[34] John T Batina. Unsteady euler airfoil solutions using unstructured dynamic meshes. *AIAA journal*, 28(8):1381–1388, 1990.

[35] Charbel Farhat, Christoph Degand, Bruno Koobus, and Michel Lesoinne. Torsional springs for two-dimensional dynamic unstructured fluid meshes. *Computer methods in applied mechanics and engineering*, 163(1-4):231–245, 1998.

[36] Chunhua Sheng and Christian B Allen. Efficient mesh deformation using radial basis functions on unstructured meshes. *AIAA journal*, 51(3):707–720, 2013.

[37] Manuel Bernard, Ghislain Lartigue, Guillaume Balarac, Vincent Moureau, and Guillaume Puigt. A framework to perform high-order deconvolution for finite-volume method on simplicial meshes. *International Journal for Numerical Methods in Fluids*, 92(11):1551–1583, 2020.

[38] Guillaume De Nayer. *Interaction Fluide-Structure pour les corps élancés*. PhD thesis, Ecole Centrale de Nantes (ECN), 2008.

[39] Emmanuel Lefrançois. A simple mesh deformation technique for fluid–structure interaction based on a submesh approach. *International Journal for Numerical Methods in Engineering*, 75(9):1085–1101, 2008.

[40] Romain Janodet, Geoffroy Vaudor, Ghislain Lartigue, Pierre Benard, Vincent Moureau, and Renaud Mercier. An unstructured conservative level-set algorithm coupled with dynamic mesh adaptation for the computation of liquid-gas flows. In *29th European Conference on Liquid Atomization and Spray Systems (ILASS Europe)*, 2019.

[41] C. Dobrzynski and P. Frey. *Anisotropic Delaunay Mesh Adaptation for Unsteady Simulations*, pages 177–194. Springer Berlin Heidelberg, 2008.

[42] P. Benard, G. Balarac, V. Moureau, C. Dobrzynski, G. Lartigue, and Y. D'Angelo. Mesh adaptation for large-eddy simulations in complex geometries. *International Journal for Numerical Methods in Fluids*, 81(12):719–740, 2015. fld.4204.

[43] Savinien Pertant, Manuel Bernard, Giovanni Ghigliotti, and Guillaume Balarac. A finite-volume method for simulating contact lines on unstructured meshes in a conservative level-set framework. *Journal of Computational Physics*, 444:110582, 2021.

[44] Andrey Pushkarev, Pierre Benard, Ghislain Lartigue, Vincent Moureau, and Guillaume Balarac. Numerical approach for simulation of moving bodies by using the dynamic mesh adaptation method within ale technique. In *ECCOMAS MSF 2017*, 2017.

[45] F Duchaine, T Morel, and A Piacentini. On a first use of cwipi at cerfacs. *Contract report TRCMGC-11-3. CERFACS*, 213, 2011.

[46] Mikel Landajuela, Marina Vidrascu, Dominique Chapelle, and Miguel A Fernández. Coupling schemes for the fsi forward prediction challenge: comparative study and validation. *International journal for numerical methods in biomedical engineering*, 33(4):e2813, 2017.

[47] Paola Causin, Jean-Frédéric Gerbeau, and Fabio Nobile. Added-mass effect in the design of partitioned algorithms for fluid–structure problems. *Computer methods in applied mechanics and engineering*, 194(42-44):4506–4527, 2005.

[48] Ulrich Küttler and Wolfgang A Wall. Fixed-point fluid–structure interaction solvers with dynamic relaxation. *Computational mechanics*, 43(1):61–72, 2008.

[49] Miguel Angel Fernández, J-F Gerbeau, and Céline Grandmont. A projection semi-implicit scheme for the coupling of an elastic structure with an incompressible fluid. *International Journal for Numerical Methods in Engineering*, 69(4):794–821, 2007.

[50] Stefan Turek and Jaroslav Hron. Proposal for numerical benchmarking of fluid-structure interaction between an elastic object and laminar incompressible flow. In *Fluid-structure interaction*, pages 371–385. Springer, 2006.

[51] Michael Schäfer, Stefan Turek, Franz Durst, Egon Krause, and Rolf Rannacher. Benchmark computations of laminar flow around a cylinder. In *Flow simulation with high-performance computers II*, pages 547–566. Springer, 1996.

[52] Stefan Turek, Jaroslav Hron, Mudassar Razzaq, Hilmar Wobker, and Michael Schäfer. Numerical benchmarking of fluid-structure interaction: A comparison of different discretization and solution approaches. In *Fluid Structure Interaction II*, pages 413–424. Springer, 2011.

[53] Andreas Kalmbach and Michael Breuer. Experimental piv/v3v measurements of vortex-induced fluid–structure interaction in turbulent flow—a new benchmark fsi-pfs-2a. *Journal of Fluids and Structures*, 42:369–387, 2013.

[54] Guillaume De Nayer, Andreas Kalmbach, Michael Breuer, Stefan Sicklinger, and Roland Wüchner. Flow past a cylinder with a flexible splitter plate: A complementary experimental–numerical investigation and a new fsi test case (fsi-pfs-1a). *Computers & Fluids*, 99:18–43, 2014.

[55] Guillaume De Nayer and Michael Breuer. Numerical fsi investigation based on les: Flow past a cylinder with a flexible splitter plate involving large deformations (fsi-pfs-2a). *International Journal of Heat and Fluid Flow*, 50:300–315, 2014.

[56] Massimo Germano, Ugo Piomelli, Parviz Moin, and William H Cabot. A dynamic subgrid-scale eddy viscosity model. *Physics of Fluids A: Fluid Dynamics*, 3(7):1760–1765, 1991.

[57] Thomas Fabbri. *Development of a high fidelity fluid-structure interaction solver: towards flexible foils simulation.* PhD thesis, Université Grenoble Alpes, 2022.